# A minimal mathematical model for polarity establishment and centralspindlin-independent cytokinesis

Ondrej Maxian, Katrina M Longhini, and Michael Glotzer

**Abstract**

The anterior-posterior axis of *Caenorhabditis elegans* embryos is determined by the position of sperm entry. The sperm-provided centrosome induces local inhibition of cortical contractility, leading to large-scale myosin flows. This process is driven by the guanine nucleotide exchange factor (GEF) ECT-2, which activates myosin through the GTPase RHO-1. Previously, we showed that in both cell polarization and cytokinesis, Aurora A (AIR-1) is activated on the centrosomes and diffuses to the cortex, where it locally inhibits ECT-2, leading to gradients in myosin concentration. These gradients in turn drive long-range flows that amplify ECT-2 asymmetries (Longhini and Glotzer, 2022). Here, we construct a mathematical model to test whether a minimal set of well characterized, essential elements are necessary and sufficient to explain the spatiotemporal dynamics of AIR-1, ECT-2, and myosin during polarization of the *C. elegans* model organism. We show that robust establishment of polarity can be obtained in response to a weak AIR-1 signal, and demonstrate the relevance of rapid ECT-2 exchange and a persistent AIR-1 cue during polarization. The tuned model also correctly predicts previously-observed ultrasensitive ECT-2 dynamics during cytokinesis, suggesting that the same minimal circuit operates in both processes.

## 1 Introduction

The anterior-posterior axis of the nematode *C. elegans* is determined in the zygote, shortly after the egg is fertilized. The position of sperm entry dictates the posterior pole (Goldstein and Hird, 1996), triggering myosin-dependent, anterior-directed cortical flows that facilitate the segregation of anterior and posterior PAR proteins into distinct domains (Munro et al., 2004; Lang and Munro, 2017; Gross et al., 2019). These cortical flows are thought to establish polarity; the PAR proteins then serve to maintain embryo polarity (Cuenca et al., 2003).

Recent studies implicated Aurora A kinase, AIR-1, as a crucial factor required to initiate these cortical flows (Klinkert et al., 2019; Kapoor and Kotak, 2019; Zhao et al., 2019; Longhini and

Glotzer, 2022). AIR-1 associates with the sperm centrosome, which is the sperm-derived structure that promotes polarity establishment (Hannak et al., 2001; Cowan and Hyman, 2004) . Recent work (Longhini and Glotzer, 2022) showed that AIR-1 impacts cortical dynamics by inhibiting ECT-2. Specifically, ECT-2 dissociates from the posterior membrane in an AIR-1 dependent manner, and it contains consensus sites for AIR-1 that are required for AIR-1 responsiveness. During polarization, ECT-2 exhibits posterior depletion and anterior enrichment, a pattern of accumulation that requires cortical myosin flows. However, unlike the anterior PAR proteins, which have residence times on the order of one hundred seconds (Robin et al., 2014), ECT-2 cannot be strongly advected, as it exchanges rapidly between the cytoplasm and the cortex on timescales of a few seconds, appearing to preferentially bind to the cortex at myosin-enriched sites (Longhini and Glotzer, 2022). Consequently, it remains unclear how a short residence time, preferential recruitment by myosin, and weak advection by cortical flows, could combine to generate the observed asymmetric accumulation of ECT-2 during polarization.

A similar set of events occur upon anaphase onset, coincident with cytokinesis (Longhini and Glotzer, 2022). At first glance, cytokinesis and polarization appear quite different, as by the time cytokinesis is reached, the centrosomes have duplicated, matured, accumulated much more AIR-1, and moved farther away from the cortex. Yet there remains a strong, ultra-sensitive dependence between the distance of the centrosome from the nearest cortical domain and the amount of cortical ECT-2 at that site; proximal centrosomes correlate with a reduction in cortical ECT-2. It is therefore possible that the same mechanisms that control polarity establishment reoccur in cytokinesis.

In this study, we test whether a minimal set of interactions can explain the dynamics of ECT-2 and myosin during both polarity establishment and centralspindlin-independent cytokinesis. To do this, we construct a mathematical model that uses an AIR-1 signal, which diffuses from the centrosomes to the cortex, as an input to a continuum model of contractility, which is similar to those previously described (Michaux et al., 2018; Gross et al., 2019). We show that our model can explain the initial dynamics of polarization, similar to those observed in the absence of PAR proteins. Furthermore, the same model reproduces the ultra-sensitive dependence of ECT-2 accumulation on centrosome distance observed during cytokinesis.

# 2 Results

## 2.1 Model formulation

### 2.1.1 Basic model of contractility

The general schematic of our model (as well as how it corresponds to the known biochemistry) is shown in Fig. 1(a), and the mathematical details are presented in Appendix B. Similar to previous studies using these types of models (Goehring et al., 2011; Dawes and Munro, 2011; Kravtsova and Dawes, 2014; Gross et al., 2019), the model geometry is one-dimensional, and can be viewed as a one-dimensional slice of the cell cortex combined with a well-mixed cytoplasm (see Fig. 1(b)). At the cortex, AIR-1 inhibits accumulation of ECT-2 by increasing its dissociation rate. The cortical pool of ECT-2 gains the ability to activate RHO-1, and consequently indirectly activate myosin. Myosin feeds back on ECT-2 by promoting its cortical recruitment (presumably indirectly), and through advection by cortical flows. Finally, there is nonlinear negative feedback of myosin accumulation (through RGA-3/4-dependent inactivation of RHO-1) (Michaux et al., 2018). For simplicity, along with many other components, we do not model the actin network, a topic for future study. To constrain unknown model parameters, we incorporate known experimental measurements for the turnover rates of each component and flow speeds, and further assume that

1. 10% of ECT-2 is bound to the cortex at steady state in wild-type embryos (see Appendix B for more details on this estimate).
2. 30% of myosin is bound to the cortex at steady state in wild-type embryos (Gross et al., 2019, Fig. S3j).
3. There is a modest increase in the recruitment rate of ECT-2 due to cortical myosin (directly or indirectly), in a myosin concentration-dependent manner, reflecting the asymmetric accumulation of ECT-2 during polarization and cytokinesis (Longhini and Glotzer, 2022). The increase in the recruitment rate was determined by fitting the pattern of ECT-2 accumulation during polarization. This behavior is qualitatively and quantitatively different from advection by flows, which has a minor effect because of short ECT-2 residence times (see Fig. S3 and (Longhini and Glotzer, 2022, Fig. 3D)).

In the Appendix, we use these assumptions to constrain the model parameters. To constrain parameters relating to contractility, we match bulk flow speeds in wild-type embryos (which are typically at most 10 $\mu$m/min) (Gross et al., 2019). Sensitivity analysis indicates that these parameters position the model on the boundary between the stable and unstable regime (Fig. S4), thus

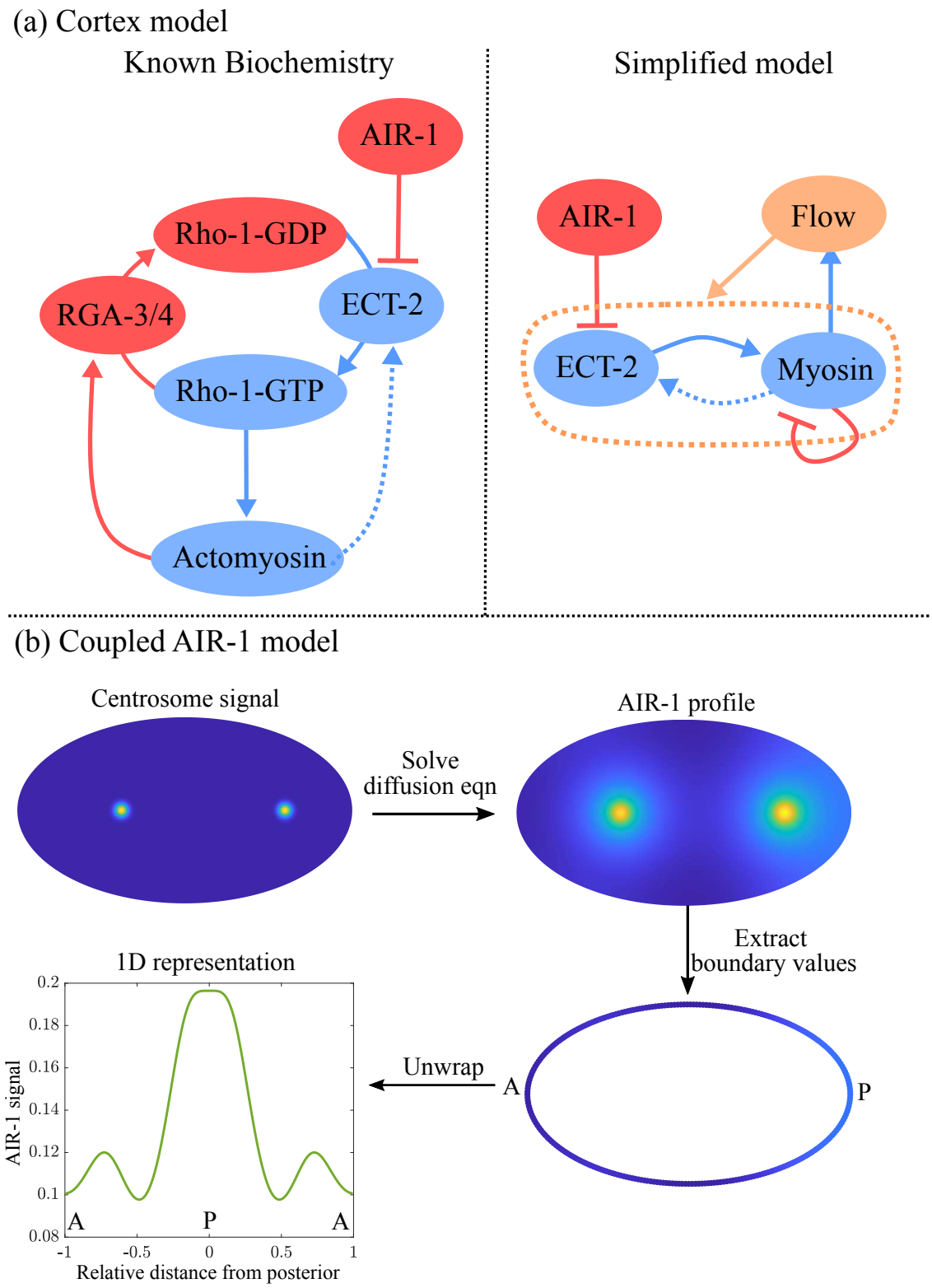


**Figure 1:** Modeling schematic for this study. (a) The model of the cortex, with the known biochemistry on the left and our simplified model on the right. This model takes the AIR-1 signal as input, and the equations are given in (S5). (b) Procedure for determining the AIR-1 signal. Given centrosome positions (shown in cytokinesis in wild-type embryos), we solve for the AIR-1 profile on the cross section using equation (S1), then formulate a one-dimensional AIR-1 profile by extracting the values on the boundary.

allowing small AIR-1 signals to be amplified without triggering contractile instabilities. While it is tempting to equate the model's myosin-driven, contractile instabilities with pulsatile Rho/myosin excitability (Nishikawa et al., 2017), the latter are actually myosin-independent (Michaux et al., 2018), which illustrates that the embryo does not sit in the model's fully unstable regime. In fact, the overall speed of bulk flows does not depend on pulsatility of Rho (Michaux et al., 2018, Fig. 7), affording a biological justification for modeling the simpler case in which these well-characterized pulses of Rho activation are absent. It was recently shown that knockdown of Rho's downstream effectors could cause contractile instabilities, which implies that the wild-type *C. elegans* embryo likely sits near, but not within, the unstable regime (Yao et al., 2022).

#### 2.1.2 Coupled model of AIR-1

As an input to the cortex model, we solve for the AIR-1 profile on the boundary (the cortex) of a two-dimensional embryo cross section. Figure 1(b) provides an overview of this process: for each embryo type, we specify the position of the centrosome(s), then solve a diffusion equation to obtain the AIR-1 profile on the entire embryo cross section. Evaluating the AIR-1 concentration (which has arbitrary units) on the boundary then gives a profile on the embryo perimeter, which we flatten out to a single periodic dimension. The mathematical details of this process are discussed in Appendix A; here it suffices to list the following assumptions that go into our model:

1. During cytokinesis, the centrosomes have radius about 1.4 $\mu$m, while during polarization the radius is about 0.35 $\mu$m (Decker et al., 2011, Fig. 1C).
2. AIR-1 is activated at centrosomes.
3. The proportion of active AIR-1 at the centrosomes during cytokinesis is 32 times that during polarization (see Fig. S5).
4. Active AIR-1 diffuses towards the cortex according to Fick's law.
5. A global phosphatase activity inactivates AIR-1 throughout the cytoplasm.
6. Once it reaches the cortex, AIR-1 inhibits ECT-2 by increasing its off rate in an AIR-1-dependent manner (see Appendix A.2 and B for equations and parameterization; our specific assumption is that, during polarization, AIR-1 increases the off-rate of ECT-2 by 10%. In wild-type cytokinesis, we compute (after accounting for diffusion and inactivation) an AIR-1 signal at the posterior that is 4 times larger (c.f. Figs. 2(b) and 4(a)), and so the off-rate in this case is enhanced by 40%).

Setting the level of global phosphatase activity is a non-trivial undertaking. As shown in Appendix

A, low levels of phosphatase activity give high global AIR-1 levels, which translate to low ECT-2 levels everywhere. Such levels were shown to block pseudocleavage in centralspindlin-independent cytokinesis, due to low contractility (Afshar et al., 2010; Kotak et al., 2016). We chose the phosphatase activity level such that centrosomes close to the posterior pole (in polarization) negligibly impact the anterior domain ($< 1\%$ of the posterior concentration); see Fig. S1.

### 2.2 The centrosome distance determines the strength of polarization

During cell polarization, the newly-duplicated centrosomes typically sit very close to the posterior cortex (about 1.9 $\mu$m away) and are small (approximate radius of 0.4 $\mu$m), as they have not yet accumulated large amounts of pericentrosomal material (Bienkowska and Cowan, 2012; Decker et al., 2011). To explore the effect of centrosome distance and location, we positioned centrosomes at a distance 1.9, 5, and 10 $\mu$m from the posterior pole, and measured the resulting AIR-1 signal by solving the diffusion equation (S1) on the embryo cross section and extracting boundary values (see schematics in Figs. 1(b) and 2(a)). As expected, there is a significant decrease in the AIR-1 signal as the distance between the centrosomes and the cell boundary increases. As compared to a 1.9 $\mu$m distance, centrosomes 5 $\mu$m from the cortex exhibit a decrease of 50% in AIR-1, and those 10 $\mu$m from the cortex exhibit a further decrease of 50% (Fig. 2(b)).

Using these profiles of AIR-1 activity, we run the model forward in time to reach a steady state for polarization. For reference, in the absence of PAR proteins, the centrosomal signal induces a transient clearing of myosin from the posterior pole, and the myosin profile reverts back to a uniform state after the centrosomes move towards the cell equator (Gross et al., 2019, Fig. 2E). Figure 2(c) shows that our simulations reproduce the initial smaller-scale clearing of both myosin and ECT-2. Under wild-type conditions, we predict a domain of ECT-2 clearance of about 30% of the half-perimeter which translates to roughly 20 $\mu$m on either side of the pole, in good agreement with experimental observations in PAR mutants (Gross et al., 2019, Fig. 2E), and close to previous measurements of 30% in embryos with a functional PAR circuit (Longhini and Glotzer, 2022, Fig. 1B, (vi)). The flow speed of at most 5–6 $\mu$m/min also matches observations in PAR mutants (Gross et al., 2019, Fig. 2G). Note that the model is calibrated (by changing the strength with which AIR-1 inhibits ECT-2) to predict an A/P asymmetry of 1.5 during polarization, which matches experimental observations (Longhini and Glotzer, 2022, Fig. 1).

In the model, changing the distance between the centrosomes and the cortex affects the quantitative values of the asymmetries and the time to reach them (Fig. 2(d)), but not the myosin

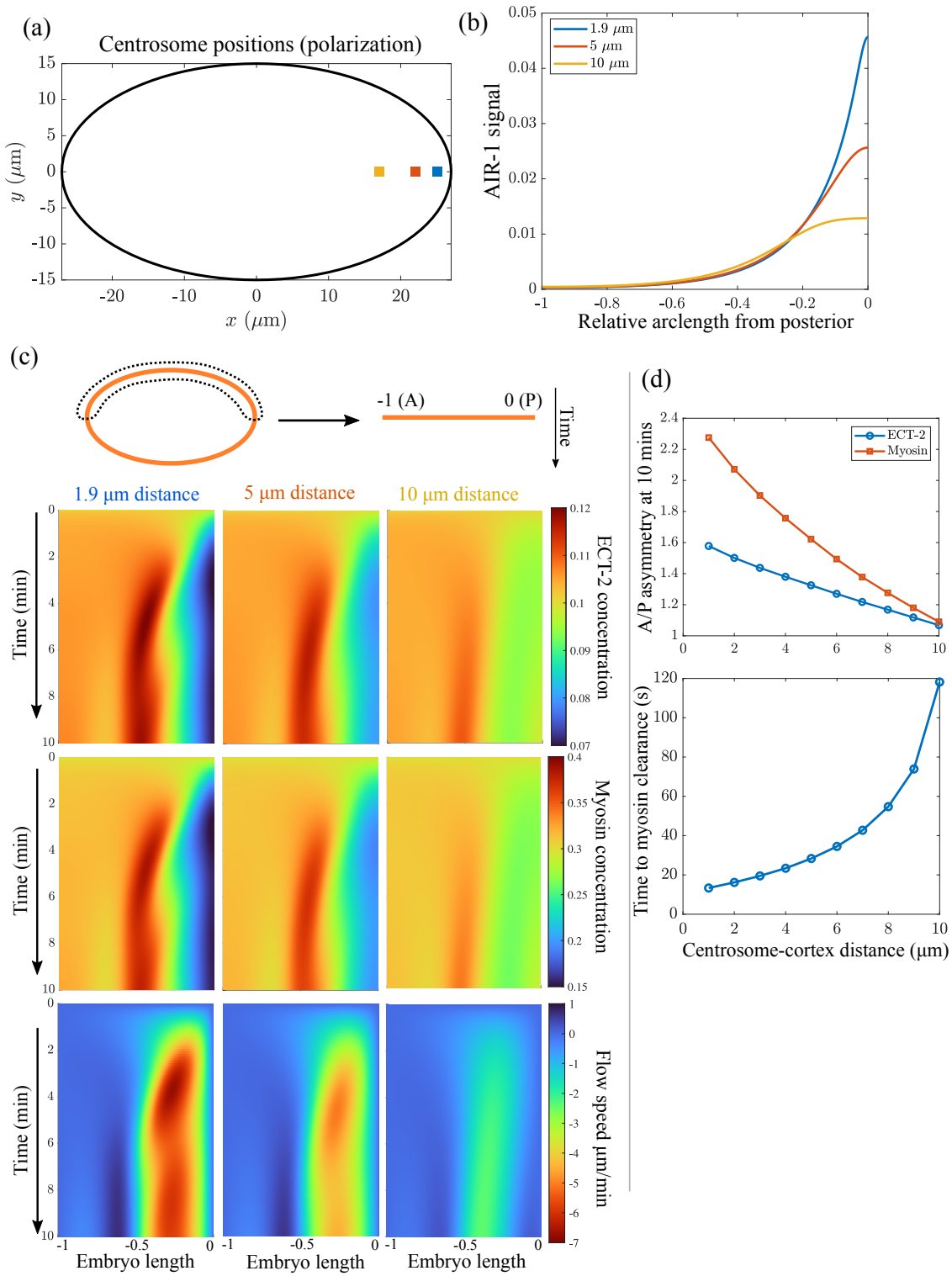


**Figure 2:** Centrosome locations set polarization dynamics. (a) The location of the centrosomes in our polarization simulations; we position both centrosomes 1.9, 5, and 10 $\mu$m away from the cell boundary. (b) The resulting AIR-1 signals along the cell perimeter. (c) The dynamics of polarization, starting from the uniform state, with the computed AIR-1 signals. We show the ECT-2 concentration (top), myosin concentration (middle), and flow speed (bottom) in pseudo-kymographs, with time on the $y$ axis, and the A/P axis on the $x$ axis (A at left and P at right). (d) The A/P asymmetry in myosin and ECT-2 after 10 mins (top) and the time for symmetry breaking (bottom), both as a function of the centrosome-cortex distance.

peak location. As shown in the kymographs in Fig. 2(c), the peak location, which correlates with the position of the pseudocleavage furrow (Reymann et al., 2016), is roughly the same across all conditions, since it is controlled by the hydrodynamic length-scale (20% of the half-perimeter). Similar to previous observations (Bienkowska and Cowan, 2012, Fig. 3F), the time for "symmetry breaking," defined as a local (10%) clearance in myosin from the posterior pole, increases from less than 20 seconds at a distance of 1 $\mu$m to about 120 seconds at a distance of 10 $\mu$m. However, our model predicts an exponential scaling of the time to symmetry breaking at very large distances; this does not match the linear trend up to 10 $\mu$m that was previously reported (Bienkowska and Cowan, 2012, Fig. 3F).

### 2.3 The relevance of rapid exchange

We have shown that long-range redistribution of ECT-2 is possible despite its short residence time. The driver of this redistribution is direct or indirect recruitment by myosin, which is longer-lived on the cortex than ECT-2. Yet, is there any benefit to having rapid turnover of ECT-2 on the cortex? To explore this question, in Fig. 3 (left two columns) we consider an alternative model in which the ECT-2 lifetime is an order of magnitude larger (without changing the percentage bound to the cortex), allowing ECT-2 to be advected, rather than recruited, by myosin (the recruitment of ECT-2 by myosin is also removed from the model). In this case, we observe contractile instabilities not seen in wild type embryos. As in control conditions, a local maximum in ECT-2 initially forms near 50% embryo length. Because of the increased residence time, however, ECT-2 is also advected *from the anterior* into the peak, which creates a local minimum in myosin and drives the formation of a second, posterior, peak. Thus the rapid exchange of ECT-2 is important in stabilizing unidirectional flows during polarization.

### 2.4 Assessing alternative polarity cues

The contractility cue that drives polarization establishment has been suggested to result from a dynein-dependent removal of myosin (Chapa-Y-Lazo et al., 2020). Although experiments have shown that polarity establishment is dynein-independent (Longhini and Glotzer, 2022), we nevertheless considered whether a transient reduction in contractility would be sufficient to trigger polarity establishment. In particular, we perform two simulations: one with the AIR-1 cue active for five minutes, and a second that lacks an AIR-1 cue but in which we acutely remove myosin and ECT-2 at the posterior pole. The resulting dynamics over ten minutes are shown in Fig. 3. In both

cases, transient cues or initial conditions ultimately relax to a steady state in which ECT-2 and myosin are nearly uniform and flow speeds are near zero. Some small, local asymmetries remain as a result of operating our model near the unstable regime (see Fig. S4).

The main difference between the transient AIR-1 cue and acute removal of myosin is in the intermediate dynamics. For a transient cue, the flow starts at zero, and steadily increases over five minutes, peaking with a flow speed of 6 $\mu$m/min. Turning off the cue causes the flow speeds to slow below 2 $\mu$m/min in $\sim$3 minutes. By contrast, unloading myosin and ECT-2 from the posterior at $t = 0$ triggers a similar set of flows towards the anterior, but the flows are maximal at $t = 1$ minute, and then steadily decrease over time. Experimental data in PAR mutants show flows that reach a maximum velocity almost immediately after polarity triggering, but the magnitude (5 $\mu$m/min) of these flows persist throughout polarity establishment phase (3–4 mins) (Gross et al., 2019, Fig. 2G). Thus, this supports models in which AIR-1 triggers a local and persistent inhibition of contractility, similar to that reported previously (Gross et al., 2019).

### 2.5 Dynamics of cytokinesis

The asymmetric accumulation of ECT-2 on the cortex during cytokinesis is sensitive to the position of the two centrosomes (Longhini and Glotzer, 2022). A plot of ECT-2 accumulation as a function of distance from the nearest cortex reveals an "S-shaped" curve; at short and long distances there is a plateau in the ECT-2 accumulation (Longhini and Glotzer, 2022, Fig. 7A). By contrast, for distances in the range 10–20 $\mu$m, there is an ultra-sensitive dependence of the ECT-2 concentration on the proximity. Note that during cytokinesis, there are two mature centrosomes which contain significantly more AIR-1 (about 30 times, Fig. S5) than the immature centrosomes that trigger polarity establishment.

To test whether the model that accurately predicts polarization recapitulates the behavior of ECT-2 during cytokinesis, we modeled the behavior of ECT-2 and myosin using the centrosome positions measured previously (Longhini and Glotzer, 2022), and repeated in Fig. 4(a). As in polarization, we solved the diffusion equaition (S1) on the embryo cross section with the given centrosome positions, then extracted the AIR-1 signal (in arbitrary units) along the cell perimeter. Figure 4(a) shows the resulting AIR-1 profiles for each of the embryo treatments, where the posterior levels of AIR-1 in *dhc-1(RNAi)* and *zyg-9(b244);tpxl-1(RNAi)* embryos clearly stand out from the rest. Despite the differences in AIR-1 signal in the posterior, these two embryo types have the same accumulation of ECT-2 (see experimental data in Fig. 4(c)). In Appendix A, we use this

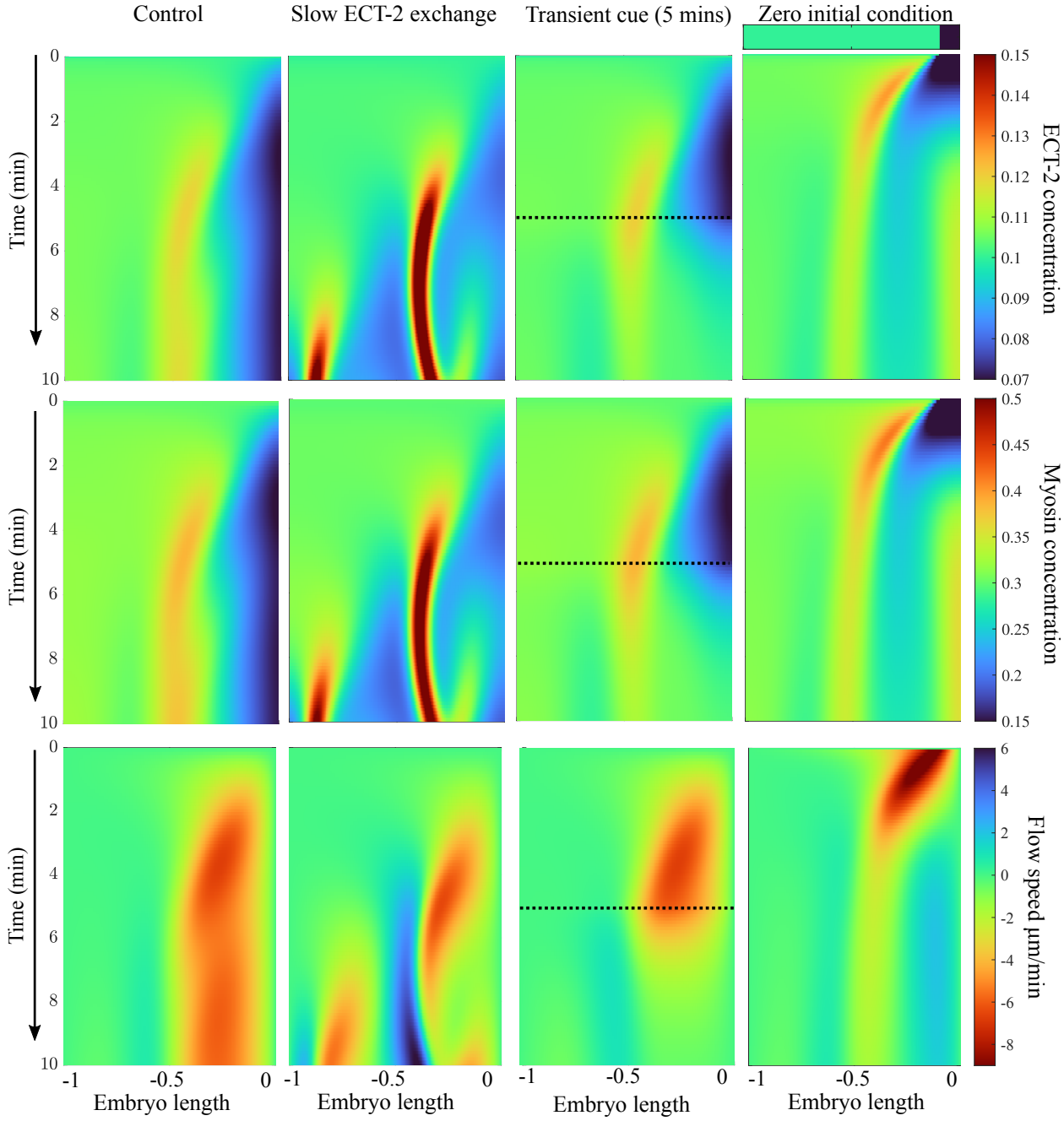


**Figure 3:** Adjusting conditions in polarization. Left panel: control parameters. Second from left: adjusting parameters so that, rather than be recruited by myosin, ECT-2 has a ten-fold longer residence time and is only advected. Third from left: Simulating the case where the AIR-1 cue is applied for five minutes (up to the dotted lines), after which we remove the AIR-1 signal and follow relaxation. Rightmost panel: Simulating the case of no AIR-1 signal, but an initial condition that has 10% of the domain at zero ECT-2 and myosin concentration (top panel shows a zoomed-in initial condition).

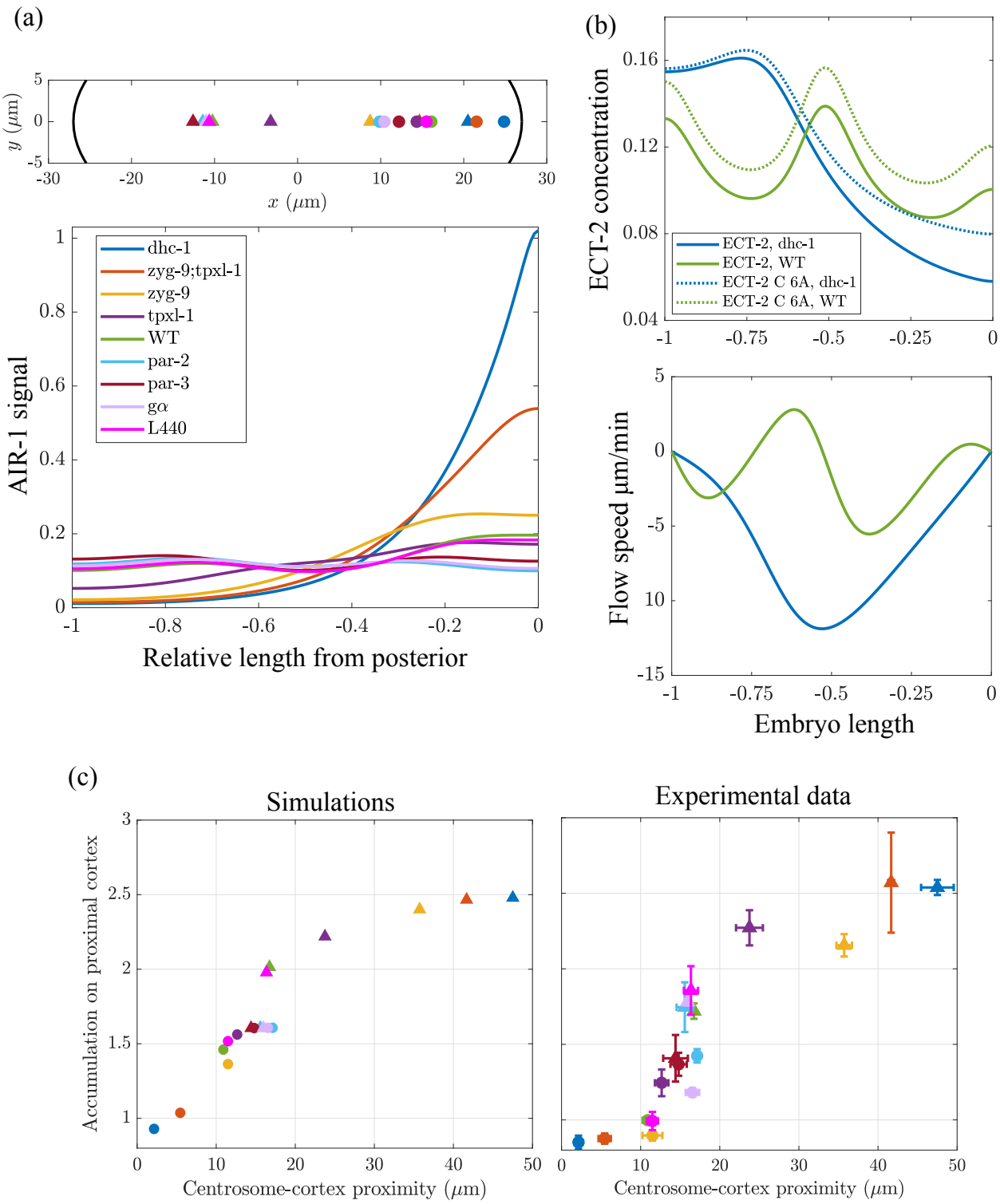


**Figure 4:** Extending the model to cytokinesis. (a) The centrosome positions for each embryo treatment, which are inputs to the diffusion model, and the corresponding AIR-1 signal on the cell perimeter, obtained from solving the diffusion equation (S1). (b) Steady states (profiles after ten minutes) in both dhc-1 (blue) and wild type (green) embryos. The dotted lines show the profile of an exogenous, inactive non-phosphorylatable version of ECT-2 which cannot interact with Rho or AIR-1. (c) The simulation results and experimental data for how the ECT-2 accumulation on the proximal cortex depends on the centrosome positions (Longhini and Glotzer, 2022, Fig. 7A); in the right panel we average the individual embryos for each of the nine treatments and show the mean values (error bars are a single standard error in the mean).

observation to inform a simple saturation model for the effect of AIR-1 on ECT-2.

We use the computed AIR-1 signals (Fig. 4(a)) as inputs to the same cortex model (Fig. 1(a)) that we parameterized under polarization conditions. Without changing any of the parameters, we simulate each embryo treatment to steady state, then record the ECT-2 concentration at the anterior/posterior pole at the time of the maximum asymmetry (approximately the steady state). Figure 4(b) shows the steady state distribution of ECT-2 and the steady state flow speeds for *dhc-1(RNAi)* and wild type embryos under cytokinesis conditions. The flows are of a realistic magnitude, and the ECT-2 concentration ratios between the anterior and posterior poles resemble experimental measurements. In addition, we also consider how this system would impact the distribution of an exogenous, inactive non-phosphorylatable version of ECT-2 (i.e., ECT-2 C 6A). The distribution of this variant in otherwise wild-type embryos (Fig. 4(b)) resembles that observed experimentally (Fig. 5D, Longhini and Glotzer (2022)), in that there is a 20% overaccumulation of ECT-2 C 6A throughout the whole embryo and no change in the A/P ratio, demonstrating that the level at which AIR-1 inhibits ECT-2 is correct in the model. Since this value was set during polarization, this suggests that the same inhibition is at play in both processes.

Finally, Figure 4(c) shows ECT-2 accumulation on the anterior/posterior pole across all embryo treatments. We observe a plateau at the low end, corresponding to saturation of the AIR-1 signal, and a plateau at the high end, where myosin accumulation and flow is inhibited by RGA-3/4. In the middle, we see an ultra-sensitive dependence: moving from 10–20 $\mu$m centrosome distance gives a roughly two-fold change in ECT-2 accumulation, similar to the experimental data. Thus our model, tuned for polarization, also reproduces the behavior during cytokinesis. This is a nontrivial undertaking; as shown in Appendix A, simpler models that do not amplify asymmetries by flow cannot reproduce the ultra-sensitive dependence for centrosome distances 10–20 $\mu$m.

## 3 Discussion

It has long been known that cell polarization in the *C. elegans* zygote is dependent on a centrosome-dependent signal that locally inhibits contractility, and that cytokinesis can be influenced by aster positioning (White, 1985; Dechant and Glotzer, 2003; Severson and Bowerman, 2003; Munro et al., 2004). Only recently, however, has a better understanding of the nature of these cues emerged (Gross et al., 2019; Kapoor and Kotak, 2019; Klinkert et al., 2019; Zhao et al., 2019; Longhini and Glotzer, 2022). In particular, a recent study (Longhini and Glotzer, 2022) showed that Aurora A

kinase, AIR-1, is activated at the centrosomes and causes inhibition of the RhoGEF ECT-2 (and, consequently, Rho and myosin) at the proximal cortex. The goal of this study was to determine if a minimal mathematical model could explain experimental observations in both polarization and cytokinesis.

We introduced a hybrid two- and one-dimensional model (Fig. 1), where the centrosome positions are obtained from experimental data, and used to obtain a cross sectional profile of AIR-1 activation. Assuming diffusion of AIR-1 to the cortex (boundary of the cross section), we then obtained the profile of AIR-1 as an input to a model of cortical contractility. This cortex model, which we defined on the cross sectional-boundary and consequently made one-dimensional, included negative feedback of AIR-1 on ECT-2 accumulation, and positive feedback of myosin on ECT-2 accumulation. The coupling of the AIR-1 and cortex models allowed the dynamics of the active cortex to be dictated by the positions of the centrosome(s). We constrained the model using experimental observations (Longhini and Glotzer, 2022) and assuming modest (at most 2-fold) effects on cortical ECT-2 by Aurora A (negatively) and myosin (positively). The parameters arising from these constraints placed the model in a regime which can amplify small signals without yielding to contractile instabilities (Yao et al., 2022).

This minimal model recapitulated almost all of the pertinent observations from polarization and cytokinesis. It produced transient polarization (in the absence of PAR proteins) with the observed characteristic flow speeds and protein ratios, and revealed the need for a *persistent* AIR-1 cue over time to maintain a polarized state in the absence of PAR reorganization. Interestingly, the model showed that a short ECT-2 residence time prevents a counterflow from the anterior end of the cell, leading to more robust anterior-directed flows during polarization. These counterflows are predicted to prevent proper establishment of polarity, an observation which could be tested experimentally.

Because the model parameters were tuned to match observations during polarization, it was most striking that the model also accurately predicted the pattern of cortical ECT-2 accumulation in centralspindlin-independent cytokinesis (Dechant and Glotzer, 2003; Verbrugghe and White, 2007; Longhini and Glotzer, 2022). Similar to recent work on contractility during cytokinesis (Werner et al., 2024), we found that the accumulation of ECT-2 in different mutants could only be explained by incorporating mechanical feedback to amplify the AIR-1/ECT-2 signal. Historically, inhibition of cortical contractility by asters was thought to be microtubule-mediated, given their proximity to the cortex (Dechant and Glotzer, 2003; Motegi et al., 2006). Yet experimental evidence (Longhini

and Glotzer, 2022) and this mathematical model indicate that centrosome position and embryo geometry (i.e., the ability for AIR-1 to diffuse from the centrosomes to the cortex) serve as the primary determinants of polar relaxation. However, as cortical interactions with astral microtubules frequently control spindle and hence centrosome positioning (Grill et al., 2001; Schaefer et al., 2000; Tame et al., 2014), a role remains for microtubules in this process.

# Supplemental text: A minimal mathematical model for polarity establishment and centralspindlin-independent cytokinesis

Ondrej Maxian, Katrina M Longhini, and Michael Glotzer

## A AIR-1 diffusion model

The contractility circuit is forced by a cue from the centrosomes which contain Aurora A (AIR-1), an inhibitor of ECT-2. We assume that the AIR-1 signal gets to the membrane by diffusion. Letting $a(\boldsymbol{x})$ be the concentration of AIR-1 in the two-dimensional embryo cross-section, we have the equation

$$\Delta a - \bar{k}^{\text{off}} a = -f \qquad \boldsymbol{x} \in \Omega. \tag{S1a}$$

$$\nabla a \cdot \boldsymbol{n} = 0 \qquad \boldsymbol{x} \in \partial\Omega, \tag{S1b}$$

where (S1a) is the diffusion equation for the concentration and (S1b) is a no-flux boundary condition through the boundary (here $\Omega$ represents the embryo area and $\partial\Omega$ represents the boundary). The signal $f(\boldsymbol{x})$ comes from the two centrosomes, which we model by Gaussian densities

$$f(\boldsymbol{x}) = \frac{C_0/D}{2\pi\sigma_c^2} \sum_{i=1}^{2} \exp\left( \frac{-\|\boldsymbol{x} - \boldsymbol{x}_i\|^2}{2\sigma_c^2} \right). \tag{S1c}$$

Here $\boldsymbol{x}_i$ is the location of the $i$th centrosome (typically at some location $(x_i, 0)$), which changes depending on the embryo conditions. In addition to the centrosome location, the signal has two other parameters: $C_0/D$ is the strength of the cue (the integral of $f(\boldsymbol{x})$ over the entire embryo cross-section, normalized by the cytoplasmic diffusion coefficient $D$), and $\sigma_c$ is the centrosome "size" (the standard deviation of the Gaussian, which is roughly half the radius of the centrosome). For cytokinesis, the centrosomes have radius about 1.4 $\mu$m (Decker et al., 2011), so we set $\sigma_c = 0.7$ $\mu$m. In polarization, the centrosomes have size about 0.35 $\mu$m, so we set $\sigma_c = 0.175$ $\mu$m. The absolute signal strength $C_0/D$ is arbitrary, but ratios between cytokinesis and polarization are well defined. Consequently, we set $C_0/D = 1$ for cytokinesis and $C_0/D = 1/32$ for polarization, according to our experimental measurements. The diffusion equation (S1a) also contains a basal rate of inactivation of AIR-1 (phosphatase activity). This introduces another parameter which is the inactivation rate relative to the diffusion coefficient in the cytoplasm ($\bar{k}^{\text{off}}$, units $\mu\text{m}^{-2}$).

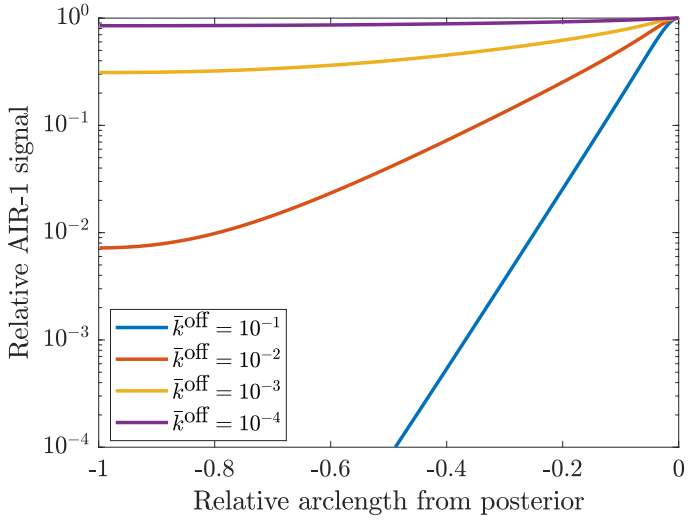


**Figure S1:** AIR-1 signal vs. distance from posterior under polarization conditions (blue squares in Fig. 2(a)). We vary the level of phosphatase activity $\bar{k}^{\text{off}}$ until the posterior level is less than 1% of the anterior level, settling on $\bar{k}^{\text{off}} = 10^{-2}$ $\mu\text{m}^{-2}$.

We use a standard first-order finite element method to solve (S1a). In brief, the elliptical domain of the embryo is meshed into nodes and triangles (Persson and Strang, 2004), and the finite element matrix equation becomes $\left(\boldsymbol{K} + \bar{k}^{\text{off}}\boldsymbol{M}\right)\boldsymbol{a} = \boldsymbol{M}\boldsymbol{f}$, where $\boldsymbol{M}$ is the mass matrix and $\boldsymbol{K}$ is the stiffness matrix for finite elements, which are assembled using standard techniques (Gockenbach, 2006, c. 7). See the github repository `https://github.com/omaxian/CElegansModel/` for code.

## A.1 Constraining level of AIR-1 phosphatase activity

To constrain the level of phosphatase activity (parameter $\bar{k}^{\text{off}}$), we compute the profile of AIR-1 under polarization conditions (both centrosomes 1.9 $\mu$m from the posterior pole (Bienkowska and Cowan, 2012)), and plot the resulting AIR-1 signal in Fig. S1. When the phosphatase activity is low, the no flux boundary condition traps AIR-1 inside the embryo, and the relative difference between posterior and anterior is small. Increasing the phosphatase activity disproportionately lowers AIR-1 levels on the anterior pole (since it is much farther from the centrosomes). We assume that anterior levels of AIR-1 during polarization are at most 1% of posterior levels; this constrains $\bar{k}^{\text{off}} = 10^{-2}$.

## A.2 Contractility-independent models for the ECT-2 response in cytokinesis

The main text demonstrated how amplfication of AIR-1 signals by flow can successfully reproduce the observed ECT-2 accumulations during cytokinesis across a variety of embryo conditions. Here

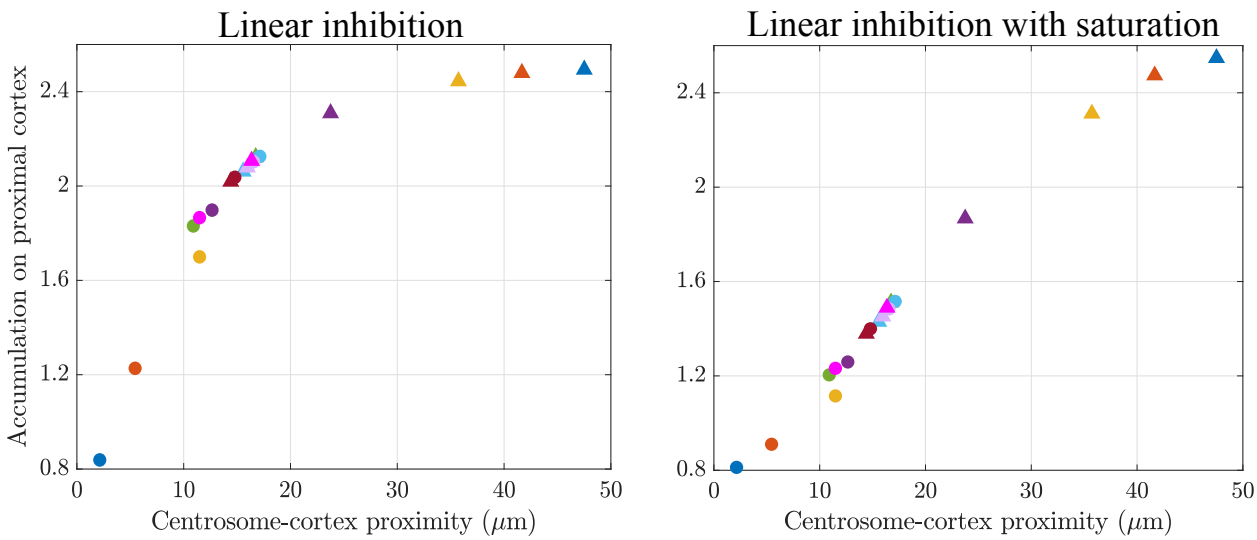


**Figure S2:** Simple models based on AIR-1/ECT-2 inhibition fail to capture the experimental data on accumulation vs. centrosome position. We consider a linear inhibition model (S3), and a linear model with saturation (S4). Compared to the data in Fig. 4, neither of these simple models capture the general S-shape of the curve, with plateaus at the low and high ends.

we consider two alternative models which *do not* include flows, in order to establish that flows are both necessary and sufficient to reproduce the experimental data.

In the simplest possible model of ECT-2 dynamics, there is a local equilibrium of the ECT-2 binding rate and unbinding rate, where the latter increases in the presence of AIR-1,

$$k_E^{\text{on}} = k_E^{\text{off}} \left(1 + K_{\text{AE}} A\right) E, \tag{S2}$$

and $K_{\text{AE}}$ expresses the strength of inhibition. This steady state model predicts that the ECT-2 concentration relates to the AIR-1 concentration at the cortex via

$$E = \frac{k_E^{\text{on}}/k_E^{\text{off}}}{1 + K_{\text{AE}} A}, \tag{S3}$$

which is a relationship with two unknown constants. Fitting these two unknown constants to the observed ECT-2 levels in *dhc-1 (RNAi)* embryos (where the AIR-1 signal is approximately 1 at the posterior and 0 at the anterior) gives $k_E^{\text{on}}/k_E^{\text{off}} = 2.55$ and $K_{\text{AE}} = 2$. Substituting the AIR-1 levels from the other embryo treatments then gives the observed centrosome/ECT-2 accumulation plot shown in the left panel of Fig. S2. There we see that the relationship (S3) correctly predicts saturation at low levels of AIR-1 (high centrosome-cortex distances), but fails to predict saturation at high AIR-1 levels (low distances) or ultra-sensitivity in between.

The AIR-1 signals we obtained in Fig. 4(a) show that the AIR-1 signal at the posterior doubles when we switch from *zyg-9 (b244);tpxl-1 (RNAi)* (red) embryos to *dhc-1 (RNAi)* embryos (blue). Yet, the experimental data in Fig. 4(c) show that the ECT-2 accumulation is unchanged. This tells us that there must be saturation in the AIR-1 inhibition dynamics; beyond some level, the amount of AIR-1 no longer impacts the inhibition strength. Based on the location of the plateau in the experimental data, it seems that this threshold level occurs around the posterior AIR-1 level in *zyg-9 (b244)* embryos, which our data in Fig. 4(a) tells us is 0.25. Thus, we propose a new model where the local equilibrium is governed by

$$k_E^{\text{on}} = k_E^{\text{off}} \left(1 + K_{\text{AE}} \left(\frac{A}{A_c + A}\right)\right) E, \tag{S4}$$

where $A_c = 0.25$. Once again fitting $k_E^{\text{on}}/k_E^{\text{off}} = 2.9$ and $K_{\text{AE}} = 3.2$ to the data for *dhc-1 (RNAi)* embryos, we obtain the centrsome/ECT-2 plot shown in the right panel of Fig. S2. This model reduces the posterior ECT-2 levels in embryos with high AIR-1 signals to approach a plateau. However, it also reduces the ECT-2 levels in the other embryos (especially *tpxl-1 (RNAi)*; purple), and we still do not see the ulta-sensitivity in distances 10–20 $\mu$m. We propose that the failure of these simple models comes from a lack of propagation of the AIR-1/ECT-2 signal via flows. As shown in Fig. 4(c), flows can exaggerate the smaller asymmetries, giving ultra sensitivity in the interior of the curve.

## B ECT-2/Myosin circuit

We formulate the equations for the model shown in Fig. 1(a), where ECT-2 (through activating RHO-1) activates myosin at the cortex. To minimze the number of parameters, we consider a simplified version of the true dynamics (where ECT-2 signals myosin by activating RHO-1) and formulate a model with two variables, $E$ (for ECT-2) and $M$ (for myosin). In dimensional units

(denoted by hats), the equations we use are

$$\partial_{\hat{t}}\hat{E} + \partial_{\hat{x}}\left(\hat{v}\hat{E}\right) = \hat{D}_E\partial_{\hat{x}}^2 E + k_E^{\text{on}}\left(1 + k_{\text{ME}}\hat{M}\right)\hat{E}_c - k_E^{\text{off}}\left(1 + k_{\text{AE}}\left(\frac{\hat{A}}{\hat{A}_c + \hat{A}}\right)\right)\hat{E} \tag{S5a}$$

$$\partial_{\hat{t}}\hat{M} + \partial_{\hat{x}}\left(\hat{v}\hat{M}\right) = \hat{D}_M\partial_{\hat{x}}^2 M + k_{\text{EM}}\hat{E}^2\hat{M}_c - k_M^{\text{off}}\hat{M} - k_{\text{fb}}\hat{M}^4 \tag{S5b}$$

$$\gamma\hat{v} = \eta\partial_{\hat{x}}^2\hat{v} + \hat{\sigma}_0\partial_{\hat{x}}\hat{M} \tag{S5c}$$

$$\hat{E}_c = \frac{1}{hL}\left(E^{(\text{Tot})}L - \int_0^L \hat{E}(\hat{x})\,d\hat{x}\right), \qquad \hat{M}_c = \frac{1}{hL}\left(M^{(\text{Tot})}L - \int_0^L \hat{M}(\hat{x})\,d\hat{x}\right). \tag{S5d}$$

Each of the species ECT-2 and myosin evolves by

1. *Advection by cortical flows.* These are the terms $\partial_x(vE)$ and $\partial_x(vM)$.
2. *Diffusion in the cortex.* These are the terms $D_E\partial_x^2 E$, and $D_M\partial_x^2 M$.
3. *Binding to the cortex.* For ECT-2, there is a basal binding rate plus a linear enhancement by myosin. For myosin, the binding rate is proportional to the square of the ECT-2 concentration, without a basal binding rate. The motivation for this term is that myosin asymmetries are typically much stronger than ECT-2 asymmetries (Longhini and Glotzer, 2022; Munro et al., 2004; Mayer et al., 2010), and thus some nonlinearity is required. We choose the minimal such nonlinearity (see (Michaud et al., 2022, Eq. (1)) for another choice, where Rho is represented explicitly). The binding rate is also proportional to the cytoplasmic concentration of each protein, defined in (S5d), where $L$ is the domain length, $h$ is the cytoplasmic "thickness" (so that $hL$ is the total area), and $A^{(\text{Tot})}$ is the concentration of protein $A$ when all of it is bound to the cortex (Lang and Munro, 2022).
4. *Unbinding from the cortex.* For ECT-2, the unbinding rate is composed of a basal rate expressing the fast exchange of ECT-2, plus inhibition by AIR-1 according to (S4). Myosin unbinds with a basal rate (expressing the combination of inactivation and unbinding), which is enhanced by additional negative feedback (the $M^4$ term). The form of this term is a coarse-grained version of previously-published work (Michaux et al., 2018). The model there considered Rho ($\rho$) and RhoGAP ($r$) as the unknowns, with the production of RhoGAP proportional to $\rho^3$ and the inhibition of $\rho$ proportional to $r\rho/(K+\rho)$. Here we coarse-grain this model into a single term, with the inhibition proportional to $M^4$.

Finally, the velocity equation (S5c) expresses the balance of active stress (which we assume is proportional to myosin concentration) with viscous stress and frictional resistance (Mayer et al., 2010).

## B.1 Dimensionless form

Because absolute concentrations are unknown, it is easiest to assign values to unknown parameters when they are in dimensionless form. To do this, we non-dimensionalize so that length is in units of the embryo perimeter $L$, time is in units of the bound myosin lifetime $1/k_M^{\text{off}}$, velocity is in units of $\sigma_0/\left(\sqrt{\eta\gamma}\right)$ (Bois et al., 2011) and concentration of species $A$ is in units of $A^{(\text{Tot})}$. This gives new dimensionless variables

$$x = \hat{x}/L \qquad t = \hat{t}k_M^{\text{off}} \qquad M = \hat{M}/M^{(\text{Tot})} \qquad E = \hat{E}/E^{(\text{Tot})} \qquad v = \hat{v}/\left(\frac{\hat{\sigma}_0}{\sqrt{\eta\gamma}}\right), \tag{S6a}$$

and a corresponding set of equations

$$\partial_t E + \sigma_0 \partial_x (vE) = D_E \partial_x^2 E + K_E^{\text{on}} (1 + K_{\text{ME}} M) E_c - K_E^{\text{off}} \left(1 + K_{\text{AE}} \left(\frac{A}{A_c + A}\right)\right) E \tag{S6b}$$

$$\partial_t M + \sigma_0 \partial_x (vM) = D_M \partial_x^2 M + K_{\text{EM}} E^2 M_c - M - K_{\text{fb}} M^4 \tag{S6c}$$

$$v = \ell^2 \partial_x^2 v + \ell \partial_x M \tag{S6d}$$

$$E_c = 1 - \int_0^1 E(x)\, dx \qquad M_c = 1 - \int_0^1 M(x)\, dx. \tag{S6e}$$

The conversion from dimensional to dimensionless form is straightforward for most of these parameters. Since some (e.g. $K_{\text{AE}}$, $K_{\text{ME}}$) are unknown anyway, it is not useful to report how they relate to the dimensional parameters. There are some important parameters to highlight, however. In flow patterns, $\ell = \left(\sqrt{\eta/\gamma}\right)/L$ is a hydrodynamic length scale (scaled by domain perimeter) expressing the connectivity of the cortex; local disturbances in myosin will typically propagate at most a distance $\ell$. The parameter $\sigma_0 = \hat{\sigma}_0/\left(Lk_M^{\text{off}}\sqrt{\eta\gamma}\right)$ expresses the strength of the flows; the dimensional velocity in $\mu$m/s can be extracted by taking $v \times \sigma_0 L k_M^{\text{off}}$.

## B.2 Numerical solution

We use standard numerical methods to solve (S6). We discretize the one-dimensional domain at $N$ points with spacing $1/\Delta x$, and define the centered differentiation matrix $\boldsymbol{D}$ and standard three-point Laplacian differentiation matrix $\boldsymbol{\Delta}$. Given the myosin profile at time step $n$, we first compute the velocity $v^{(n)}$ by solving $v^{(n)} = \ell^2 \boldsymbol{\Delta} v^{(n)} + \ell \boldsymbol{D} M^{(n)}$. Once the velocity is computed, the ECT-2 and myosin equations are solved by combining a first-order upwind finite volume scheme for the advection terms (Hundsdorfer et al., 2003, Sec. 1.4) with implicit treatment of the diffusion

terms (using the standard three point Laplaian). The reaction terms are all treated explicitly, and time-stepping is first-order accurate. Matlab code is available at the github repository `https://github.com/omaxian/CElegansModel/`.

### B.3 Parameter estimation

Some of the parameters, as listed below, can be determined directly from experimental measurements,

1. The embryo cross section is an ellipse with approximate radii 27 $\mu$m and 15 $\mu$m, which gives a perimeter $L = 134.6$ $\mu$m (Goehring et al., 2011) .
2. The variable $\ell$ is the hydrodynamic length scale. In dimensional units, this was measured to be approximately 13 $\mu$m (Mayer et al., 2010), which means $\ell = 0.1$ in (S6) (10% domain perimeter).
3. The myosin bound lifetime is about 15 s, so $k_M^{\text{off}} = 1/15$ s$^{-1}$. This is 1.5 times longer than the estimate for single molecules (Nishikawa et al., 2017; Gross et al., 2019) to reflect the more long-lived nature of myosin foci during establishment phase (Munro et al., 2004).
4. We assume that all species have a dimensional diffusion coefficient $\hat{D}_{E/M} = 0.1$ $\mu$m$^2$/s (Goehring et al., 2011; Gross et al., 2019; Robin et al., 2014). Rescaling length by $L$ and time by $k_M^{\text{off}}$ gives a dimensionless coefficient $D_E = D_M = 0.1/(L^2 k_M^{\text{off}}) = 4.6 \times 10^{-5}$.
5. The ECT-2 lifetime was measured using FRAP to be on the order of a few seconds (Longhini and Glotzer, 2022, Fig. 3D). In cytokinesis, we set $k_E^{\text{off}} = 0.33$/s, for a three second lifetime. Rescaling gives $K_E^{\text{off}} = k_E^{\text{off}}/k_M^{\text{off}} = 5$. The data show slightly faster recovery during polarization, so we increase $k_E^{\text{off}}$ by 20% for those simulations.
6. For the negative feedback of myosin, we use the parameters determined in (Michaux et al., 2018). The feedback strength is obtained by assuming an equilibrium of RhoGAP in those equations (neglecting the basal binding rate), which gives (in their notation)

$$K_{\text{fb}} = k_{\text{GAP}} \left( k_r^{\text{ass}} / k_r^{\text{diss}} \right) = 0.1(0.245/0.047) = 0.52/\text{s}.$$

   Rescaling by $k_M^{\text{off}}$ gives $K_{\text{fb}} = 7.8$ in our model.

These assumptions give values for all parameters except for $K_E^{\text{on}}$, $K_{\text{ME}}$, $K_{\text{AE}}$, $A_c$, $K_{\text{EM}}$, and $\sigma_0$. Four of these parameters can be fit by considering the desired model behavior in the absence of AIR-1. Experimental data (Longhini and Glotzer, 2022, Fig. 1) show that the A/P ECT-2 ratio

is about 1.5:1, and that 10% of ECT-2 is bound to the cortex. This estimate is based on imaging which revealed the intensity in the cortical region to be 1.5 times the cytoplasm (Longhini and Glotzer, 2022, Fig. 1). If the embryo is an ellipsoid with radii $27 \times 15 \times 15$ $\mu$m and the cortex has thickness 400 nm, then the cortex is 6.7% of the total volume. Multiplying by 1.5 gives 10% of the total ECT-2 bound. While the specific number (10%) is of little consequence to our model, the relative abundance of ECT-2 in the cytoplasm demonstrates that cytoplasmic depletion will not play a role in the dynamics. A similar set of data (Gross et al., 2019, Figs. S2,S3) show that the A/P myosin ratio is about 2:1, with 30% of myosin is bound to the cortex, and cortical flows on the order 10 $\mu$m/min.

Figure S3 shows how we incorporate these data to fix the simulation parameters. First, as shown in the top panels, we fix the ECT-2 profile according to experimental observations, then adjust $K_{\mathrm{EM}} = 50$ and $\sigma_0 = 0.2$, so that at steady state we obtain the myosin profile and flow speeds observed in experiments. Similarly, in the bottom panels, we fix the myosin profile to correspond to experimental measurements, then adjust the parameters $K_E^{\mathrm{on}}$ and $K_{\mathrm{ME}}$ until we obtain the correct ECT-2 profile. In particular, in each case we set $K_E^{\mathrm{on}}$ so that 10% of ECT-2 is bound to the cortex. Setting $K_{\mathrm{ME}} = 0$ (with $K_E^{\mathrm{on}} = 0.66$) gives no recruitment of ECT-2 by myosin, and the ECT-2 profile is only shaped by advection, and is consequently barely asymmetric. Increasing to $K_{\mathrm{ME}} = 10/9$ (with $K_E^{\mathrm{on}} = 0.5$) gives about 25% of ECT-2 recruited by myosin and a larger asymmetry. We settle on $K_{\mathrm{ME}} = 10/3$ (with $K_E^{\mathrm{on}} = 0.34$), which gives 50% of ECT-2 recruited by myosin, and the 1.5:1 A/P ratio we seek. This completes the selection of all parameters, except for $K_{\mathrm{AE}}$ and $A_c$.

Throughout this paper, we treat the simulated value at the anterior ($x = 0, 1$) and posterior ($x = 0.5$) poles as the cortical concentration that can be compared with experiments. As such, to select $K_{\mathrm{AE}} = 0.5$, we enforce that the ECT-2 ratio at the $E(0.5)/E(0) \approx 1.5$ under normal polarization conditions (left panel of Fig. 2). The threshold $A_c$ cannot be fit from polarization conditions because AIR-1 signals are low; as such we set its value according to the investigation in Appendix A.2 ($A_c = 0.25$).

### B.3.1 Parameter adjustments: polarization

In Fig. 3, we modify the parameters to examine an alternative hypothesis where ECT-2 has a longer lifetime. We consider in particular $k_E^{\mathrm{off}} = 1/25$ s$^{-1}$ (25 s residence time instead of 2.5) and $K_E^{\mathrm{on}} = 0.068$ (to give 10% bound ECT-2), and $K_{\mathrm{ME}} = 0$, so that myosin doesn't recruit ECT-2.

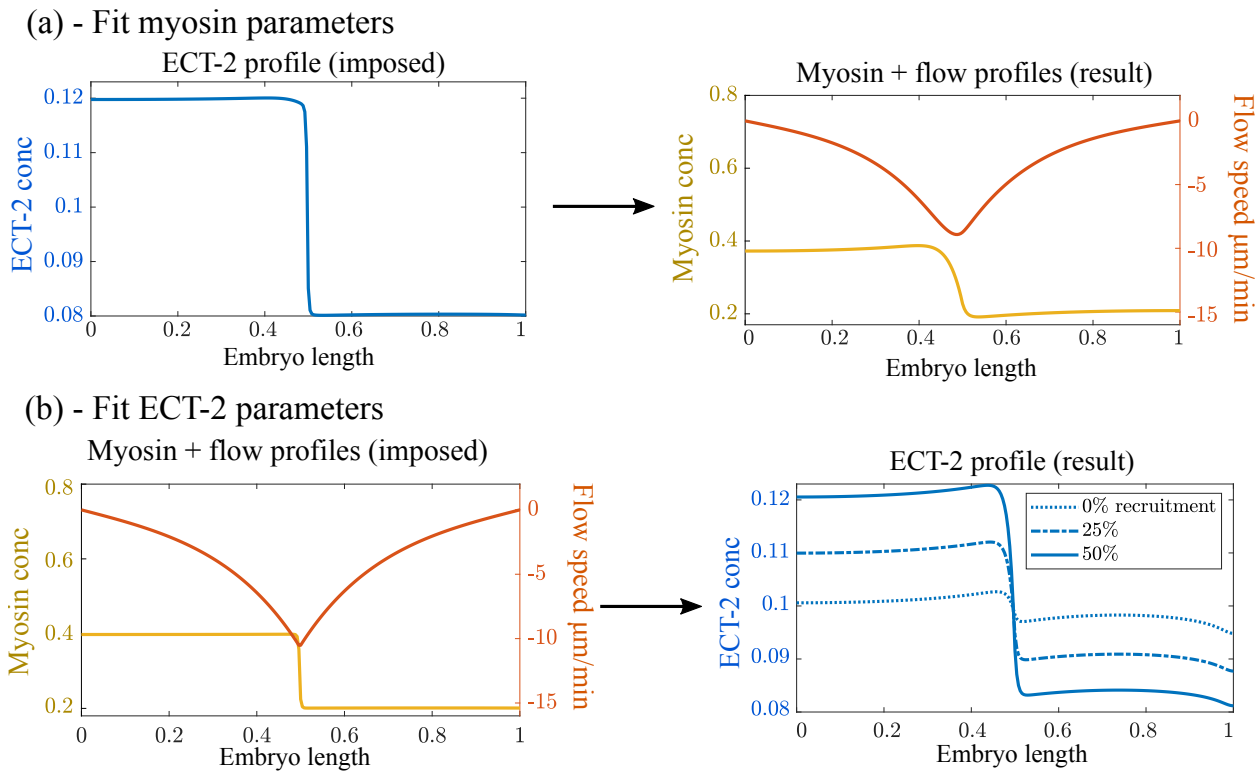


**Figure S3:** Validating our simple model of the cell cortex and setting the parameters. Top panels: we impose an ECT-2 profile that is 50% higher on the anterior than posterior, then measure the myosin and flow profiles with our chosen parameters. Bottom panels: we impose the myosin and corresponding flow profile, and examine the ECT-2 profiles with different rates of myosin recruitment.

All other parameters take their default values.

### B.3.2 Equation for ECT-2 C 6A

In Fig. 4, we consider an exogenous variant of ECT-2 which cannot interact with Rho and AIR-1, but can associate with cortical myosin. Denoting this species by $\widetilde{E}$, its evolution equation is (c.f. (S6b))

$$\partial_t \widetilde{E} + \sigma_0 \partial_x \left( v \widetilde{E} \right) = D_E \partial_x^2 \widetilde{E} + K_E^{\text{on}} \left( 1 + K_{\text{ME}} M \right) \widetilde{E}_c - K_E^{\text{off}} \widetilde{E}. \tag{S7}$$

The parameters ($\sigma_0, D_E, K_E^{\text{on}}, K_E^{\text{off}}$, and $K_{\text{ME}}$) take the same values as for the wild-type copy of ECT-2.

## B.4 Linear stability analysis of model equations

To perform linear stability analysis of the model equations (S6) with $K_{\text{AE}} = 0$, we perturb the myosin and ECT-2 profiles around the uniform state by setting $M = M_0 + \delta M$ and $E = E_0 + \delta E$, where $\delta M = \sum_k m_k(t) \exp(2\pi i k x)$, and likewise for $\delta E$. Substituting this representation for $M$ into the velocity equation (S6d) then gives a representation for the velocity $v = \sum_k v_k(t) \exp(2\pi i k x)$, where (Bois et al., 2011, Eq. (11))

$$v_k(t) = \frac{2\pi i k \ell m_k(t)}{1 + (2\pi k \ell)^2}. \tag{S8}$$

Substituting this representation into the ECT-2 and myosin equations, and keeping terms to linear order in $\delta$ gives the matrix equation

$$\frac{d}{dt} \begin{pmatrix} m_k \\ e_k \end{pmatrix} = \begin{pmatrix} \dfrac{M_0 \sigma_0 (2\pi k)^2 \ell}{1 + (2\pi k \ell)^2} - (2\pi k)^2 D_M - 1 - 4 M_0^3 K_{\text{fb}} & 2 K_{\text{EM}} E_0 (1 - M_0) \\ \dfrac{E_0 \sigma_0 (2\pi k)^2 \ell}{1 + (2\pi k \ell)^2} & -(2\pi k)^2 D_E - K_E^{\text{off}} \end{pmatrix} \begin{pmatrix} m_k \\ e_k \end{pmatrix}. \tag{S9}$$

The dynamics are unstable if the $2 \times 2$ matrix above has a positive eigenvalue (negative determinant).

The stability diagram in Fig. S4 shows the number of unstable modes for each pair $(\sigma_0, \ell)$, with all other (biochemical) parameters fixed to their default values. The most unstable behavior (quantified by how many of the first 10 Fourier modes $k = 1, \ldots 10$ in (S9) are unstable) occurs for high flow speeds and small length-scales, so that disturbances remain localized but still generate large flows. We group the stability behavior into three regimes: fully stable (region 1), partially

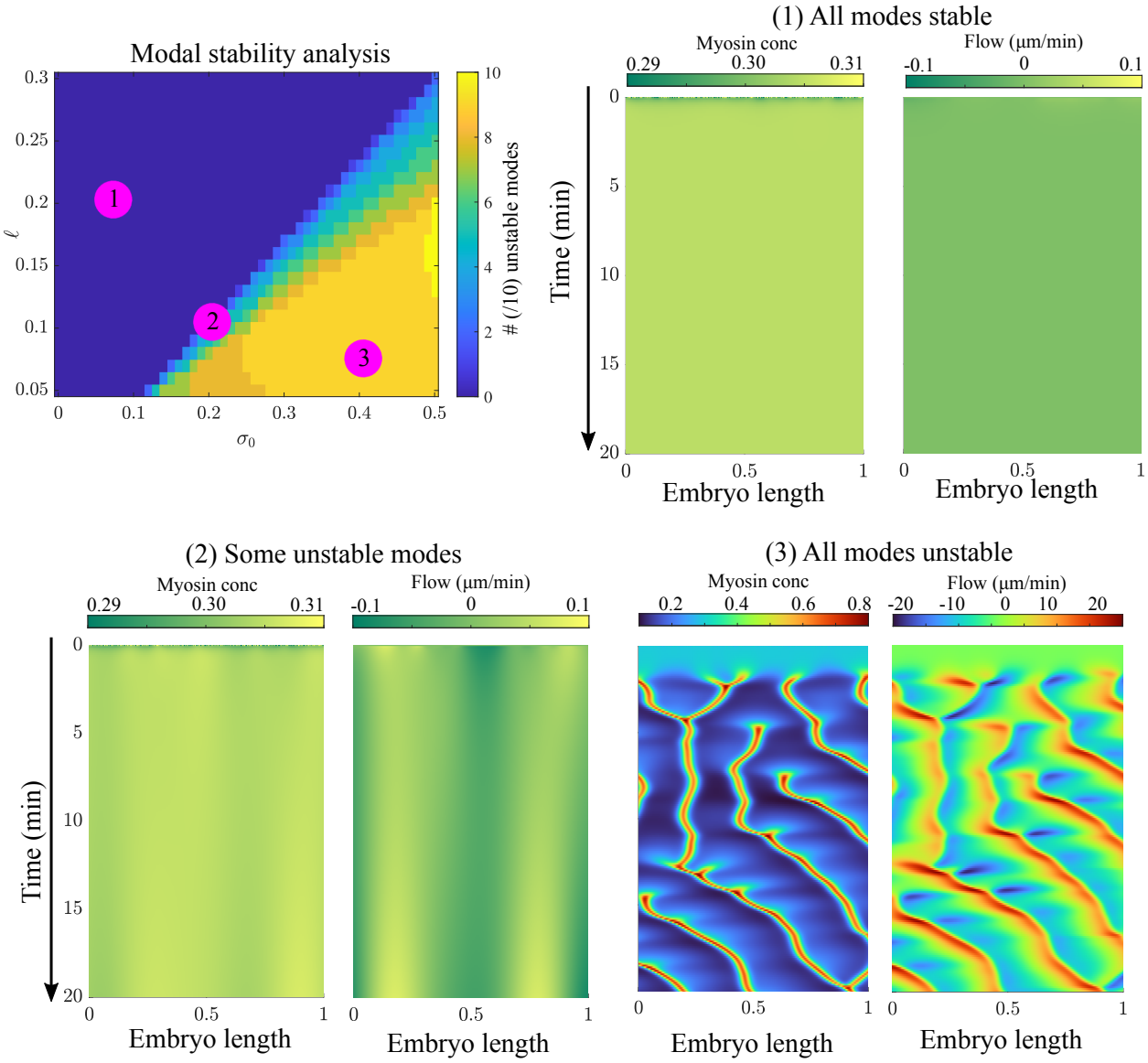


**Figure S4:** Linear stability analysis of the uniform state, and resulting types of model behavior. (Top left) Number (out of the first ten) of unstable modes in stability analysis. (1) When all modes are stable, perturbations decay back to the uniform state. (2) When some modes are unstable, perturbations in some wavelengths are amplified, while others decay. Our model falls in this regime. (3) When all modes are unstable, contractile instabilities form and combine.

(un)stable (region 2), and fully unstable (region 3). In the stable regime, all disturbances decay to the uniform steady state almost immediately, while in the intermediate regime, some of the modes are unstable, resulting in an overall pattern of contractility which slowly grows over time (although the "growth" is zero for all practical purposes). In the unstable regime, we see the formation of a steady state number of contractile peaks, which are advected throughout the domain by the flows they generate. The spacing between the pulses is controlled by the hydrodynamic length scale; in Fig. S4, the length-scale is 8% of the perimeter, or 16% of the half perimeter (which we call the embryo length). Thus, when two pulses become 32% embryo length ($2 \times$ the hydrodynamic length-scale) apart, a "dead zone" emerges between the pulses that cannot "feel" either pulse. Instabilities there give rise to a new pulse. This process repeats, so that at "steady" state, the number of pulses is set by the spacing of $2\ell$.

Fitting the parameters from wild type embryos places our bulk flow model in regime 2 (in fact, the parameters marked with "2" in Fig. S4 correspond exactly to those we use). Indeed, being close to the unstable regime without being in it allows the system to robustly amplify small AIR-1 cues without forming hyper-contractile peaks of activity that we see in the unstable regime. There is experimental evidence that wild-type *C. elegans* embryos operate near the unstable regime, as knocking down downstream effectors of Rho can lead to contractile instabilities (Yao et al., 2022).

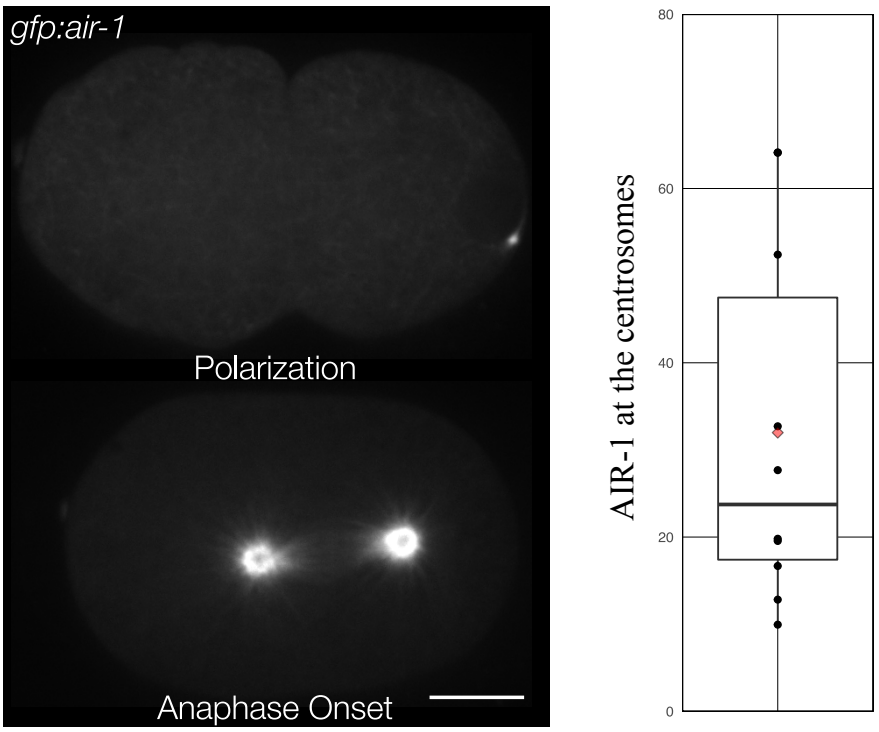


**Figure S5:** AIR-1 accumulation at the centrosomes is increased at anaphase onset relative to polarization. Representative stills of an embryo at polarization and anaphase onset show accumulation of AIR-1 at the centrosomes (*C. elegans* strain: MOT272). The graph plots the amount of AIR-1 at anaphase onset relative to polarization, which has mean 32 ($n = 10$). The black circles represent individual embryos and the red diamond is the mean.

## References

Katayoun Afshar, Michael E Werner, Yu Chung Tse, Michael Glotzer, and Pierre Gönczy. Regulation of cortical contractility and spindle positioning by the protein phosphatase 6 pph-6 in one-cell stage c. elegans embryos. *Development*, 137(2):237–247, 2010.

Dominika Bienkowska and Carrie R Cowan. Centrosomes can initiate a polarity axis from any position within one-cell c. elegans embryos. *Current biology*, 22(7):583–589, 2012.

Justin S Bois, Frank Jülicher, and Stephan W Grill. Pattern formation in active fluids. *Biophysical Journal*, 100(3):445a, 2011.

Bernardo Chapa-Y-Lazo, Motonari Hamanaka, Alexander Wray, Mohan K Balasubramanian, and Masanori Mishima. Polar relaxation by dynein-mediated removal of cortical myosin ii. *J Cell Biol*, 219(8):1250, 2020.

Carrie R Cowan and Anthony A Hyman. Centrosomes direct cell polarity independently of microtubule assembly in c. elegans embryos. *Nature*, 431(7004):92–96, 2004.

Adrian A Cuenca, Aaron Schetter, Donato Aceto, Kenneth Kemphues, and Geraldine Seydoux. Polarization of the c. elegans zygote proceeds via distinct establishment and maintenance phases. *Development*, 130(7):1255–1265, 2003.

Adriana T Dawes and Edwin M Munro. Par-3 oligomerization may provide an actin-independent mechanism to maintain distinct par protein domains in the early caenorhabditis elegans embryo. *Biophysical journal*, 101(6):1412–1422, 2011.

Reinhard Dechant and Michael Glotzer. Centrosome separation and central spindle assembly act in redundant pathways that regulate microtubule density and trigger cleavage furrow formation. *Dev Cell*, 4(3):333–344, 2003.

Markus Decker, Steffen Jaensch, Andrei Pozniakovsky, Andrea Zinke, Kevin F O'Connell, Wolfgang Zachariae, Eugene Myers, and Anthony A Hyman. Limiting amounts of centrosome material set centrosome size in c. elegans embryos. *Current Biology*, 21(15):1259–1267, 2011.

Mark S Gockenbach. *Understanding and implementing the finite element method*. SIAM, 2006.

Nathan W Goehring, Philipp Khuc Trong, Justin S Bois, Debanjan Chowdhury, Ernesto M Nicola, Anthony A Hyman, and Stephan W Grill. Polarization of par proteins by advective triggering of a pattern-forming system. *Science*, 334(6059):1137–1141, 2011.

B Goldstein and S N Hird. Specification of the anteroposterior axis in caenorhabditis elegans. *Development*, 122(5):1467–1474, 1996.

S W Grill, P Gönczy, E H Stelzer, and A A Hyman. Polarity controls forces governing asymmetric spindle positioning in the caenorhabditis elegans embryo. *Nature*, 409(6820):630–633, 2001.

Peter Gross, K Vijay Kumar, Nathan W Goehring, Justin S Bois, Carsten Hoege, Frank Jülicher, and Stephan W Grill. Guiding self-organized pattern formation in cell polarity establishment. *Nature physics*, 15(3):293–300, 2019.

Eva Hannak, Matthew Kirkham, Anthony A Hyman, and Karen Oegema. Aurora-a kinase is required for centrosome maturation in caenorhabditis elegans. *The Journal of cell biology*, 155 (7):1109–1116, 2001.

Willem H Hundsdorfer, Jan G Verwer, and WH Hundsdorfer. *Numerical solution of time-dependent advection-diffusion-reaction equations*, volume 33. Springer, 2003.

Sukriti Kapoor and Sachin Kotak. Centrosome aurora a regulates rhogef ect-2 localisation and ensures a single par-2 polarity axis in c. elegans embryos. *Development*, 146(22):dev174565, 2019.

Kerstin Klinkert, Nicolas Levernier, Peter Gross, Christian Gentili, Lukas von Tobel, Marie Pierron, Coralie Busso, Sarah Herrman, Stephan W Grill, Karsten Kruse, et al. Aurora a depletion reveals centrosome-independent polarization mechanism in caenorhabditis elegans. *Elife*, 8:e44552, 2019.

Sachin Kotak, Katayon Afshar, Coralie Busso, and Pierre Gönczy. Aurora a kinase regulates proper spindle positioning in c. elegans and in human cells. *Journal of cell science*, 129(15):3015–3025, 2016.

Natalia Kravtsova and Adriana T Dawes. Actomyosin regulation and symmetry breaking in a model of polarization in the early caenorhabditis elegans embryo: symmetry breaking in cell polarization. *Bulletin of mathematical biology*, 76:2426–2448, 2014.

Charles F Lang and Edwin Munro. The par proteins: from molecular circuits to dynamic self-stabilizing cell polarity. *Development*, 144(19):3405–3416, 2017.

Charles F Lang and Edwin M Munro. Oligomerization of peripheral membrane proteins provides tunable control of cell surface polarity. *Biophysical Journal*, 121(23):4543–4559, 2022.

Katrina M Longhini and Michael Glotzer. Aurora a and cortical flows promote polarization and cytokinesis by inducing asymmetric ect-2 accumulation. *Elife*, 11:e83992, 2022.

Mirjam Mayer, Martin Depken, Justin S Bois, Frank Jülicher, and Stephan W Grill. Anisotropies in cortical tension reveal the physical basis of polarizing cortical flows. *Nature*, 467(7315):617–621, 2010.

Ani Michaud, Marcin Leda, Zachary T Swider, Songeun Kim, Jiaye He, Jennifer Landino, Jenna R Valley, Jan Huisken, Andrew B Goryachev, George von Dassow, et al. A versatile cortical pattern-forming circuit based on rho, f-actin, ect2, and rga-3/4. *Journal of Cell Biology*, 221(8): e202203017, 2022.

Jonathan B Michaux, François B Robin, William M McFadden, and Edwin M Munro. Excitable rhoa dynamics drive pulsed contractions in the early c. elegans embryo. *Journal of Cell Biology*, 217(12):4230–4252, 2018.

Fumio Motegi, Nathalie V Velarde, Fabio Piano, and Asako Sugimoto. Two phases of astral microtubule activity during cytokinesis in c. elegans embryos. *Developmental cell*, 10(4):509–520, 2006.

Edwin Munro, Jeremy Nance, and James R Priess. Cortical flows powered by asymmetrical contraction transport par proteins to establish and maintain anterior-posterior polarity in the early c. elegans embryo. *Developmental cell*, 7(3):413–424, 2004.

Masatoshi Nishikawa, Sundar Ram Naganathan, Frank Jülicher, and Stephan W Grill. Controlling contractile instabilities in the actomyosin cortex. *Elife*, 6:e19595, 2017.

Per-Olof Persson and Gilbert Strang. A simple mesh generator in matlab. *SIAM review*, 46(2): 329–345, 2004.

Anne-Cécile Reymann, Fabio Staniscia, Anna Erzberger, Guillaume Salbreux, and Stephan W Grill. Cortical flow aligns actin filaments to form a furrow. *elife*, 5:883, 2016.

François B Robin, William M McFadden, Baixue Yao, and Edwin M Munro. Single-molecule analysis of cell surface dynamics in caenorhabditis elegans embryos. *Nature methods*, 11(6): 677–682, 2014.

M Schaefer, A Shevchenko, and J A Knoblich. A protein complex containing inscuteable and the galpha-binding protein pins orients asymmetric cell divisions in drosophila. *Curr Biol*, 10(7): 353–362, 2000.

Aaron F Severson and Bruce Bowerman. Myosin and the par proteins polarize microfilament-dependent forces that shape and position mitotic spindles in caenorhabditis elegans. *The Journal of cell biology*, 161(1):21–26, 2003.

Mihoko Tame, Jonne Raaijmakers, Bram van den Broek, Arne Lindqvist, Kees Jalink, and René H Medema. Astral microtubules control redistribution of dynein at the cell cortex to facilitate spindle positioning. *Cell Cycle*, 13(7):1162–1170, 2014.

Koen J C Verbrugghe and John G White. Cortical centralspindlin and g alpha have parallel roles in furrow initiation in early c. elegans embryos. *J Cell Sci*, 120(Pt 10):1772–1778, 2007.

Michael E Werner, Dylan D Ray, Coleman Breen, Michael F Staddon, Florian Jug, Shiladitya Banerjee, and Amy Shaub Maddox. Mechanical and biochemical feedback combine to generate complex contractile oscillations in cytokinesis. *Current Biology*, 2024.

JG White. The astral relaxation theory of cytokinesis revisited. *BioEssays*, 2(6):267–272, 1985.

Baixue Yao, Seth Donoughe, Jonathan Michaux, and Edwin Munro. Modulating rhoa effectors induces transitions to oscillatory and more wavelike rhoa dynamics in caenorhabditis elegans zygotes. *Molecular Biology of the Cell*, 33(6):ar58, 2022.

Peng Zhao, Xiang Teng, Sarala Neomi Tantirimudalige, Masatoshi Nishikawa, Thorsten Wohland, Yusuke Toyama, and Fumio Motegi. Aurora-a breaks symmetry in contractile actomyosin networks independently of its role in centrosome maturation. *Dev Cell*, 48(5):631–645.e6, 2019.